

Random-Flux-Induced Topological Phase Transitions and Chern Insulators

Chang-An Li,^{1,*} Bo Fu,^{2,†} Jian Li,³ and Björn Trauzettel^{1,4,‡}

¹*Institute for Theoretical Physics and Astrophysics,
University of Würzburg, 97074 Würzburg, Germany*

²*School of Sciences, Great Bay University, Dongguan 523000, Guangdong, China*

³*Department of Physics, School of Science, Westlake University, Hangzhou 310024, Zhejiang, China*

⁴*Würzburg-Dresden Cluster of Excellence ct.qmat, Germany*

(Dated: November 18, 2024)

We study the relevance of random flux on stability and emergence of topological phases of matter. A particularly interesting model in the presence of random flux is the anisotropic Wilson-Dirac model in two spatial dimensions. We show that this model exhibits an intriguing topological phase transition from a weak topological insulator to a Chern insulator driven by random flux. We numerically establish a global phase diagram of this model in presence of random flux. We uncover the underlying mechanism of topological phase transitions with an analytical effective medium theory, illustrating momentum-dependent renormalizations of model parameters by random flux. This analysis allows us to identify quasi-critical phase points at transitions between weak and strong topological phases, where eigen states are extended in one spatial direction but localized in the other one. Our results describe a qualitatively new effect of disorder on topological phases of matter.

Introduction.- Disorder plays a pivotal role in various physical phenomena, such as Anderson transitions [1, 2], quantum Hall effect [3, 4], and quantum transport [5]. In the realm of topological phases of matter [6, 7], the interplay between disorder and topology gives rise to novel topological phase transitions and the emergence of topological Anderson insulators [8–28]. While disorder manifests in many forms, it is typically understood as random potentials following certain statistics. Most studies on the impact of disorder in topological physics have focused on on-site disorder, i.e., scalar potential fluctuations. Random flux, which genuinely introduces fluctuations in the vector potential, represents a distinct class of disorder. It has been extensively studied in context of the fractional quantum Hall effect [29] and electron localization [30–45], but its influence on topological phases of matter remains largely unexplored. As such, an intriguing open question is whether random flux can induce novel topological phase transitions, resulting in random-flux-driven topological nontrivial phases.

In this work, we study the effect of random flux in a two-dimensional (2D) anisotropic Wilson-Dirac (AWD) model that belongs to the unitary symmetry class [46]. This model describes Chern insulators (CIs) [47], as well as normal insulators (NIs) and weak topological insulators (WTIs) [see Fig. 1(a)]. We investigate the emerging topological phase transitions driven by random flux applied to the 2D model [see Fig. 1(b)]. We establish a global phase diagram in parameter space depicted in Fig. 1(c), which shows how random flux modifies the topological phases in the clean limit. Remarkably, topological CIs can be induced from WTIs by random flux, signaled by the emergent nonzero Bott index and quantized conductance. Intriguingly, such phase transitions are marked by quasi-critical phase points, at which the localization length is divergent in one direction but finite in the other

one. We develop an effective medium theory of random flux, which illustrates the mechanism of topological phase transitions by renormalizations of model parameters due to multiple scattering processes.

2D anisotropic Wilson-Dirac model.- We consider the 2D AWD model with the Bloch Hamiltonian

$$H(\mathbf{k}) = (m + \sum_{i=x,y} b_i \cos k_i) \sigma_z + \sum_{i=x,y} v_i \sin k_i \sigma_i, \quad (1)$$

where $\sigma_{x,y,z}$ are Pauli matrices for orbital degrees of freedom and $\mathbf{k} \equiv (k_x, k_y)$ is the Bloch wave vector of Dirac electrons. Here, m (mass term), b_i , and v_i are model parameters. The anisotropy of this model arises from the choice $b_x \neq b_y$ and $v_x \neq v_y$. It is a generalization of the Qi-Wu-Zhang model [47].

The phase diagram in terms of Chern numbers is shown in Fig. 1(a). Notably, an additional phase with $C = 0$ emerges for $|m| < |b_x - b_y|$ if $b_x \neq b_y$. The new phase can be interpreted as a WTI [48–50], which is essentially trivial in 2D but fully characterized by topological indices in 1D [51]. This contrasts with the isotropic model, where the Chern number exhibits a direct transition between $C = \pm 1$ [47].

Applying random flux to the model.- We apply random flux to the AWD model in 2D real space. As illustrated in Fig. 1(b), a magnetic flux with random value $\phi(\mathbf{r})$ is enclosed within each plaquette of the square lattice, where $\mathbf{r} = (x, y)$ denotes the lattice coordinates. The random value $\phi(\mathbf{r})$ is uniformly distributed within $[-U_d/2, U_d/2]$ with U_d the random flux strength [33–35, 41]. The random flux affects the Hamiltonian through a vector potential $\mathbf{A}(\mathbf{r})$ via the Peierls substitution [52].

Upon introducing random flux into the system, standard methods for calculating Chern numbers fail. Instead, we employ the Bott index B , which has been

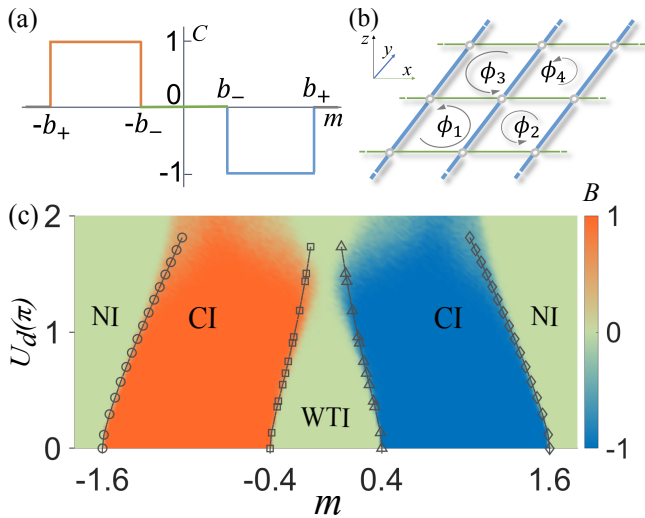


Figure 1. (a) Chern number as a function of mass m for the AWD model in the clean limit. We define $b_{\pm} \equiv |b_x \pm b_y|$, with the assumptions $b_+ > b_-$ and $v_x v_y > 0$. (b) Schematic of adding random flux to the AWD model on a square lattice. Thin green and thick blue lines indicate anisotropic bonds along x and y directions, respectively. Here, $\phi_{i=\{1,2,3,4\}}$ exemplify the random fluxes. (c) Phase diagram of the AWD model in the presence of random flux. It illustrates the Bott index as a function of random flux strength U_d and mass m . The dash-dot lines indicate the phase boundaries obtained from effective medium theory, where the markers (circle, square, triangle, and diamond) represent gap-closing at HSPs Γ , Y , X , and M , respectively. Other parameters are: $b_x = 1$, $b_y = 0.6$, $v_x = 0.2$, and $v_y = 1$. The system size is $L_x \times L_y = 30 \times 30$ with periodic boundary conditions. We average over 120 random flux configurations.

proven to be equivalent to the Chern number [53]. The Bott index is defined as [54]

$$B = \frac{1}{2\pi} \text{Im} \text{Tr} [\log(\tilde{U}_y \tilde{U}_x \tilde{U}_y^\dagger \tilde{U}_x^\dagger)], \quad (2)$$

where \tilde{U}_x and \tilde{U}_y are the reduced matrices of $U_x = P e^{i2\pi \hat{x}/L_x} P$ and $U_y = P e^{i2\pi \hat{y}/L_y} P$ in the occupied space [55], respectively. In the above formula, $\hat{x}(\hat{y})$ is the position operator along the $x(y)$ dimension and $L_x(L_y)$ is the corresponding size, and P is the projection operator constructed by the occupied states in a column-wise packing way.

Phase diagram modified by random flux.- The phase diagram in terms of the Bott index, as depicted in Fig. 1(c), illustrates the main results of our work. It shows how random flux affects the topological phases as compared to the clean case as shown in Fig. 1(a). This modification is nontrivial in the sense that topological phase regimes with $B = \pm 1$ (corresponding to $C = \pm 1$) can expand towards trivial regimes by random flux and vice versa.

We examine the modified phase boundaries between different insulating phases, focusing on the region $m <$

0. The location of the CI/NI boundary is initially at $m = -b_+$. As U_d increases, this boundary gradually shifts toward the CI side. This result indicates that CIs are robust against weak random flux and that the well-established topological Anderson phase transitions from NIs to CIs do not appear in the presence of random flux [8, 10]. The CI/WTI boundary shows a similar tendency but with richer features. It first gradually invades the WTI side and then fades away. Remarkably, the WTI with $C = 0$ can be driven to a CI with $C = +1$, which sharply contrasts with the on-site disorder scenario. Typically, strong topological phases are driven to WTIs by on-site disorders [13]. Indeed, we observe that under on-site potential disorder, the corresponding phase boundaries of the AWD model bend in the opposite direction. In addition, we note that the anisotropy from Fermi velocity ratio v_x/v_y also plays an important role in determining phase boundaries [51]. All of these features suggest new mechanisms for topological phase transitions induced by random flux. They are addressed in the following sections.

Random-flux-induced topological Chern insulators and corresponding transport signatures.- We further illustrate the influence of random flux more closely by examining the change of Bott index and corresponding transport signatures. For CIs at small U_d , the Bott index remains well-quantized, indicating the robustness of CIs against random flux, as shown in Fig. 2(a). When U_d becomes sufficiently strong, a topological phase transition occurs, and the Bott index drops to zero. For WTIs with an initial Chern number $C = 0$, however, the Bott index increases from $B = 0$ to a plateau of $B = +1$ as U_d increases, then drops to zero gradually [see Fig. 2(b)]. This indicates that the WTI with $C = 0$ is driven into a CI with $C = +1$. Consequently, it realizes a random-flux-induced topological CI, which we term topological random-flux insulator (TRFI) in the following.

The chiral edge modes corresponding to nonzero Chern numbers give rise to quantized conductances. To this end, we calculate the two-terminal conductance using the Landauer-Büttiker formalism [56, 57]. Upon introducing random flux, the conductance $G = \frac{e^2}{h}$ survives weak random flux for CIs until a topological phase transition occurs, as shown in Fig. 2(c). More intriguingly, for TRFIs, the conductance increases from zero to a plateau $G = \frac{e^2}{h}$ as increasing U_d [see Fig. 2(d)], consistent with topological phase transitions observed in Fig. 2(b). The emergent conductance plateau signals the formation of chiral edge modes driven by random flux. This quantized conductance is robust against on-site disorder, reinforcing the topological nature of TRFIs [51].

Mechanism of random-flux-induced topological phase transitions.- Topological phase transitions are typically characterized by gap-closing and reopening. In the clean limit, the AWD model respects an inversion symmetry

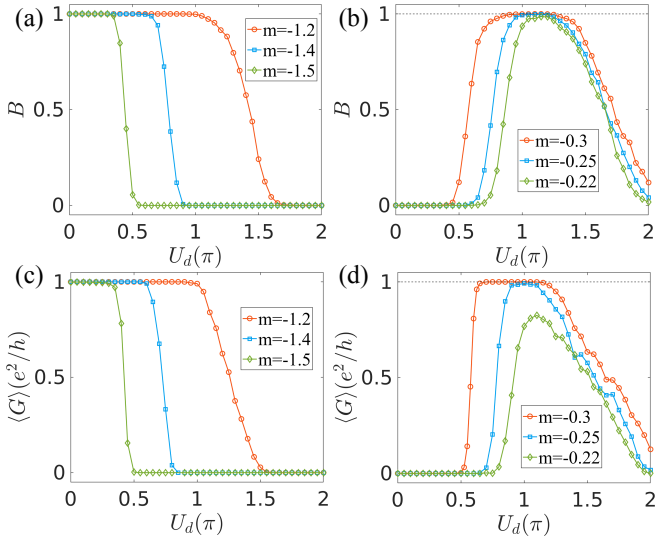


Figure 2. (a) and (b): Bott index as a function of U_d for different mass m , corresponding to the phase diagram in Fig. 1(c) averaging over 1280 random flux configurations. (c) and (d): Averaged two-terminal conductance along x direction as a function of U_d corresponding to (a) and (b), respectively. Here, the system size is $L_x \times L_y = 200 \times 200$, the Fermi energy is $E = 0$, and we average over 200 random flux configurations.

$\mathcal{P}H(\mathbf{k})\mathcal{P}^{-1} = H(-\mathbf{k})$ with $\mathcal{P} = \sigma_z$. The Chern number is then directly related to the parity of the occupied bands at four high-symmetry points (HSPs) via the relation $(-1)^C = \prod_{j=1}^4 \xi_j(K_j)$, where $K_{1,2,3,4} \equiv \Gamma, X, M, Y$, respectively, and $\xi_j = \pm 1$ represents the parity eigenvalue [50]. When the gap closes and reopens, the effective mass at the HSPs changes sign, flipping the corresponding parities and, consequently, altering the Chern number. For $C = 0$, however, the Chern number does not distinguish between NIs and WTIs. To resolve this, we introduce two weak Z_2 indices (ν_x, ν_y) which allow us to identify WTIs. These indices are defined by $(-1)^{\nu_x} = \xi_1 \xi_2$ and $(-1)^{\nu_y} = \xi_1 \xi_4$ [51]. The AWD model thereby distinguishes three distinct phases for $C = 0$ by $(C; \nu_x \nu_y) = (0; 00), (0; 01),$ and $(0; 10)$, respectively, where $(0; 00)$ corresponds to NIs and the two others correspond to WTIs [51].

To uncover the physical mechanism underlying random-flux-induced topological phase transitions, we derive an effective Hamiltonian by averaging over random flux configurations. We average a large number ($\sim 10^5$) of random flux configurations such that the translation and inversion symmetries are effectively restored. The averaged Green's function is expressed as $G_{\text{avg}}^r(\mathbf{r} - \mathbf{r}', E) = \langle G^r(\mathbf{r}, \mathbf{r}', E) \rangle$, where $\langle \dots \rangle$ denotes the average over random flux configurations. Performing a Fourier transformation on the averaged Green's function $G^r(\mathbf{k}, E) = \sum_{\mathbf{r}} G_{\text{avg}}^r(\mathbf{r}, E) e^{i\mathbf{k} \cdot \mathbf{r}}$, we construct an effective Hamiltonian $H_{\text{eff},G}(\mathbf{k}) = -[G^r(\mathbf{k}, E = 0)]^{-1}$. It en-

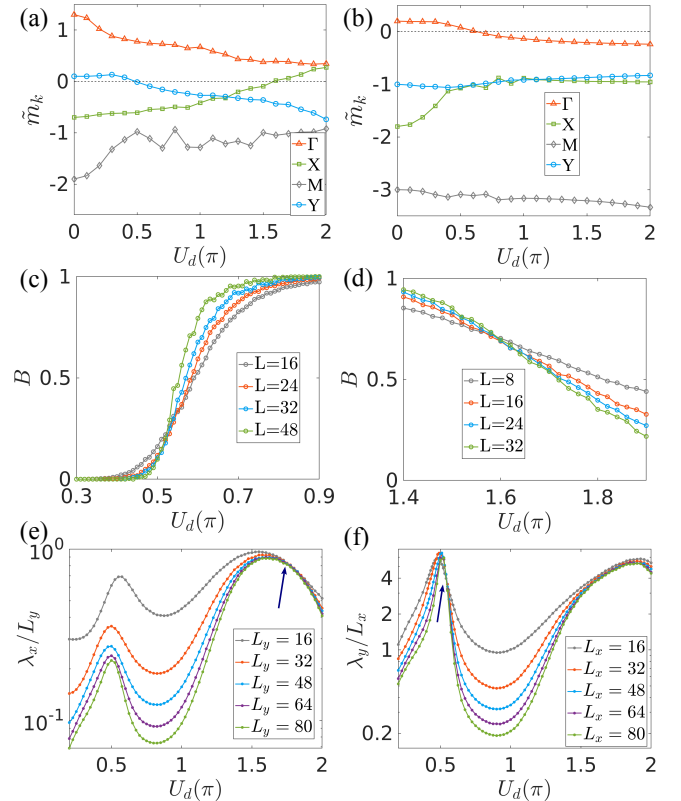


Figure 3. (a) Renormalized mass at the HSPs obtained from the effective Hamiltonian $H_{\text{eff},G}(\mathbf{k})$ with $m = -0.3$. (b) The same as (a) but with $m = -1.4$. Here, 4×10^5 random flux configurations are averaged. (c) and (d): Scaling of Bott index as a function of U_d . (e) and (f): Localization length λ_x and λ_y as a function of U_d on a quasi-1D tube of length 2×10^6 , where $L_{x/y}$ indicates the width (circumference). Other parameters are: $m = -0.3, b_x = 1, b_y = 0.6, v_x = 0.2,$ and $v_y = 1$.

ables us to extract the effective mass terms and determine the parity configurations at HSPs, shedding light on the topological phase transitions induced by random flux.

Specifically, we take the emergence of TRFIs as an example, depicted in Fig. 3(a). In the clean limit with $m = -0.3$, the effective masses at HSPs have $\tilde{m}_{\Gamma, Y} > 0$ and $\tilde{m}_{X, M} < 0$, corresponding to a WTI with $(C; \nu_x \nu_y) = (0; 10)$. Introducing random flux results in different renormalization of the effective masses at four HSPs. At the Y point, \tilde{m}_Y decrease to zero at around $U_{d1} \simeq 0.5\pi$, and continues to decrease, signaling a gap-closing transition. As U_d increases further, \tilde{m}_X gradually shifts from negative to positive values, indicating another gap-closing transition at X near $U_{d2} \simeq 1.6\pi$. Between U_{d1} and U_{d2} , the system enters the TRFI. In contrast, the masses at the other two HSPs remain unchanged, with $\tilde{m}_\Gamma > 0$ and $\tilde{m}_M < 0$ throughout the process. Accompanying these transitions, the parity indicator $\xi \equiv \begin{pmatrix} \xi_4 & \xi_3 \\ \xi_1 & \xi_2 \end{pmatrix}$ evolves as

$\xi : \begin{pmatrix} - & + \\ - & + \end{pmatrix} \rightarrow \begin{pmatrix} + & + \\ - & + \end{pmatrix} \rightarrow \begin{pmatrix} + & + \\ - & - \end{pmatrix}$, which leads to the topological index transition $(C; \nu_x \nu_y) = (0; 10) \rightarrow C = 1 \rightarrow (C; \nu_x \nu_y) = (0; 01)$. While in a different scenario, where $m = -1.4$, as shown in Fig. 3(b), only \tilde{m}_Γ flips its sign at around $U_{d3} \simeq 0.6\pi$, and the system is driven from a CI to a NI with $C = 1 \rightarrow (C = 0; 00)$. These results align with the phase diagram in Fig. 1(c) and transport signatures in Figs. 2(c) and 2(d), respectively. We further analyze the scaling behavior of the Bott index in Figs. 3(c) and 3(d). As the system size L increases, the Bott index exhibits opposite trends on either side of phase critical points. These points align with the gap-closing transitions in Fig. 3(a), reinforcing the connection between phase transitions and the renormalized masses at HSPs.

Quasi-critical phase point.— The plateau transition $C : 0 \leftrightarrow 1$ typically marks a critical phase point where the localization length diverges [4]. In Figs. 3(e) and 3(f), we plot the renormalized localization lengths [14, 58] corresponding the transitions in Fig. 3(a). Notably, we observe pronounced spatial anisotropy in the localization behavior: At the transition point U_{d1} , the localization length λ_y diverges in the thermodynamic limit, while λ_x is finite. This indicates that the states at this critical phase point are extended in y direction but remain localized in the x direction. In contrast, at the transition point U_{d2} , λ_x diverges while λ_y becomes finite. We identify these phase transitions points as “quasi-critical phase points”, characterized by anisotropic localization behavior along two spatial directions. This phenomenon is interpreted as a consequence of topological phase transitions between CIs and WTIs with anisotropy, reflected by topological index transitions $(C; \nu_x \nu_y) = (0; 10) \leftrightarrow C = 1 \leftrightarrow (C; \nu_x \nu_y) = (0; 01)$. We note that such quasi-critical phase points are absent in the transition between CIs and NIs [51].

Effective medium theory.— A more comprehensive understanding of the random-flux-induced topological phase transitions can be achieved through an effective medium theory. Central to this approach is the self-energy contribution arising from the random flux scattering, which modifies the original Hamiltonian. After applying random flux, we can express the full Hamiltonian as $\hat{H} = \hat{H}_0 + \hat{V}[\mathbf{A}(\mathbf{r})]$, where \hat{H}_0 is the Hamiltonian in the clean limit and $\hat{V}[\mathbf{A}(\mathbf{r})]$ is the perturbative potential. Note that the variance of the vector potential is $\langle A_\alpha(\mathbf{q}) A_\beta(-\mathbf{q}) \rangle = D_{\alpha\beta}(\mathbf{q})$ and we have defined $D_{\alpha\beta}(\mathbf{q}) \equiv \frac{U_d^2}{12} \frac{\delta_{\alpha\beta} - \hat{q}_\alpha \hat{q}_\beta}{|\mathbf{q}|^2}$ with $\hat{q}_\alpha \equiv q_\alpha / |\mathbf{q}|$ [59].

We calculate the self-energy following the Feynman diagrams as shown in Fig. 4. We begin by considering the diamagnetic corrections, which involve closed scattering lines [see Fig. 4(a)]. After random flux averaging, only the terms containing even orders of $A_\alpha(\mathbf{k})$ survive. The self-consistent Dyson equation is given by $G^r(\mathbf{k}, \mathbf{k}', E) = \delta_{\mathbf{k}\mathbf{k}'} G_0^r(\mathbf{k}, E) +$

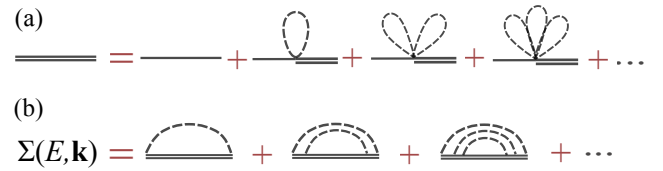


Figure 4. (a) Dyson equation of Dirac electrons being scattered by random flux. The single (double) line indicates the bare (dressed) Green’s function of electrons and dashed lines indicate the scattering by vector potential A . (b) Self-energy calculation using a self-consistent approach under the non-crossing approximation.

$G_0^r(\mathbf{k}, E) \sum_{\mathbf{k}''} V(\mathbf{k}, \mathbf{k}'') G^r(\mathbf{k}'', \mathbf{k}', E)$, where G_0^r (G^r) denotes the retarded Green’s function in absence (presence) of random flux [60]. Consequently, the correction resulting from the diamagnetic effect is evaluated as $\Sigma_{\text{DM}}(\mathbf{k}) = \langle V(\mathbf{k}, \mathbf{k}) \rangle = J_{\alpha\alpha}(\mathbf{k}) [1 - e^{-\frac{1}{2\nu} \sum_{\mathbf{q}} D_{\alpha\alpha}(\mathbf{q})}]$ where $J_{\alpha\alpha}(\mathbf{k}) \equiv \frac{\partial^2 H(\mathbf{k})}{\partial k_\alpha \partial k_\alpha}$ [51]. Notably, the exponential form of this correction term indicates an infinite order of diamagnetic terms. Incorporating these corrections, the model parameters in Eq. (1) are renormalized to $\tilde{b}_\alpha = b_\alpha e^{-\frac{1}{2\nu} \sum_{\mathbf{q}} D_{\alpha\alpha}(\mathbf{q})}$ and $\tilde{v}_\alpha = v_\alpha e^{-\frac{1}{2\nu} \sum_{\mathbf{q}} D_{\alpha\alpha}(\mathbf{q})}$. This renormalization effectively renders electrons to be ‘dressed’ by random flux. We observe that \tilde{b}_α decreases as U_d increases, which qualitatively accounts for renormalization trends of effective masses in Figs. 3(a) and 3(b).

We proceed to calculate the self-energy using the dressed Green’s function under a non-crossing approximation [see Fig. 4(b)]. Considering all diagrams with lowest-order non-crossing impurity lines, it yields the self-consistent approximation of the self-energy:

$$\Sigma(E, \mathbf{k}) = \int_{BZ} \frac{d^2 q}{(2\pi)^2} D_{\alpha\beta}(\mathbf{q}) \Gamma_\alpha(\mathbf{k}, \mathbf{k} - \mathbf{q}) \times \frac{1}{E - \tilde{H}(\mathbf{k} - \mathbf{q}) - \Sigma(E, \mathbf{k} - \mathbf{q})} \Gamma_\beta(\mathbf{k} - \mathbf{q}, \mathbf{k}), \quad (3)$$

where $\tilde{H}(\mathbf{k} - \mathbf{q})$ denotes the Hamiltonian modified by the diamagnetic correction. The vertex term is defined as $\Gamma_\alpha(\mathbf{k}, \mathbf{k}') \equiv \frac{1}{2} [J_\alpha(\mathbf{k}) + J_\alpha(\mathbf{k}')]$. After incorporating the self-energy $\Sigma(E, \mathbf{k})$, this approach can quantitatively account for the modified phase boundaries of the AWD model in the presence of random flux. As shown in Fig. 1(c), we determine four phase boundaries by imposing gap closing condition at Γ, X, Y and M . All these phase boundary lines coincide with the ones obtained from numerically calculating Bott index. Therefore, our effective medium theory explains the underlying mechanism of topological phase transitions by momentum-dependent renormalizations of model parameters, which arises from the diamagnetic effect and multiple scatterings of random flux. Notably, this mechanism clearly distinguishes

from that of on-site disorder induced topological physics corresponding to a global mass shift [10].

Discussion and conclusion.— To summarize, we have demonstrated the random-flux-induced topological phase transitions and emergence of TRFIs within the AWD model in 2D. We have established a global phase diagram based on the Bott index, further verified by both bulk and boundary descriptions thereof in terms of transport signatures, parity indicators, and effective band structures. We have developed an effective medium theory to account for the influence of random flux, which explains the modified phase diagram through a renormalization of model parameters. Moreover, we have identified quasi-critical phase points driven by random flux, characterized by anisotropic localization behavior.

The realization of random flux is feasible in different physical platforms such as electric circuits [61], photonic crystals [62], Rydberg atoms [42], and ultracold atoms [63, 64]. Therefore, we anticipate that the random-flux-induced topological phase transitions are experimentally observable. Our results could also apply to 3D systems and systems of higher Chern numbers. A generalization of random flux with $U(1)$ nature to non-Abelian $SU(2)$ gauge fields is an interesting direction of future research.

We thank Professor Shun-Qing Shen for helpful discussion. C.A.L. thanks Nicolas Bauer and Philipp Heilmann for help on computational resources. This work was supported by the DFG (SPP 1666, SFB 1170 ToCoTronics, and SFB 1143 (project A04, Project-Id 247310070)), and the Würzburg-Dresden Cluster of Excellence ct.qmat, EXC 2147 (Project-Id 390858490). We thank the Bavarian Ministry of Economic Affairs, Regional Development and Energy for financial support within the High-Tech Agenda Project “Bausteine für das Quanten Computing auf Basis topologischer Materialien.” B.F. is financially supported by Guangdong Basic and Applied Basic Research Foundation No. 2024A1515010430 and No. 2023A1515140008. J.L. acknowledges the support from NSFC under Project No. 92265201 and the Innovation Program for Quantum Science and Technology under Project No. 2021ZD0302704.

* changan.li@uni-wuerzburg.de

† fubo@gbu.edu.cn

‡ trauzettel@physik.uni-wuerzburg.de

- [1] P. W. Anderson, “Absence of diffusion in certain random lattices”, *Phys. Rev.* **109**, 1492 (1958).
- [2] F. Evers and A. D. Mirlin, “Anderson transitions”, *Rev. Mod. Phys.* **80**, 1355 (2008).
- [3] H. P. Wei, D. C. Tsui, M. A. Paalanen, and A. M. M. Pruisken, “Experiments on delocalization and universality in the integral quantum hall effect”, *Phys. Rev. Lett.* **61**, 1294 (1988).
- [4] M. Onoda and N. Nagaosa, “Quantized anomalous hall effect in two-dimensional ferromagnets: Quantum hall effect in metals”, *Phys. Rev. Lett.* **90**, 206601 (2003).
- [5] Y. V. Nazarov and Y. M. Blanter, *Quantum Transport: Introduction to Nanoscience* (Cambridge University Press, 2006).
- [6] M. Z. Hasan and C. L. Kane, “*Colloquium* : Topological insulators”, *Rev. Mod. Phys.* **82**, 3045 (2010).
- [7] X.-L. Qi and S.-C. Zhang, “Topological insulators and superconductors”, *Rev. Mod. Phys.* **83**, 1057 (2011).
- [8] J. Li, R.-L. Chu, J. K. Jain, and S.-Q. Shen, “Topological anderson insulator”, *Phys. Rev. Lett.* **102**, 136806 (2009).
- [9] H. Jiang, L. Wang, Q.-f. Sun, and X. C. Xie, “Numerical study of the topological anderson insulator in hgte/cdte quantum wells”, *Phys. Rev. B* **80**, 165316 (2009).
- [10] C. W. Groth, M. Wimmer, A. R. Akhmerov, J. Tworzydło, and C. W. J. Beenakker, “Theory of the topological anderson insulator”, *Phys. Rev. Lett.* **103**, 196805 (2009).
- [11] H.-M. Guo, G. Rosenber, G. Refael, and M. Franz, “Topological anderson insulator in three dimensions”, *Phys. Rev. Lett.* **105**, 216601 (2010).
- [12] E. Prodan, “Three-dimensional phase diagram of disordered hgte/cdte quantum spin-hall wells”, *Phys. Rev. B* **83**, 195119 (2011).
- [13] K. Kobayashi, T. Ohtsuki, and K.-I. Imura, “Disordered weak and strong topological insulators”, *Phys. Rev. Lett.* **110**, 236803 (2013).
- [14] A. Yamakage, K. Nomura, K.-I. Imura, and Y. Kuramoto, “Criticality of the metal–topological insulator transition driven by disorder”, *Phys. Rev. B* **87**, 205141 (2013).
- [15] I. Mondragon-Shem, T. L. Hughes, J. Song, and E. Prodan, “Topological criticality in the chiral-symmetric aiii class at strong disorder”, *Phys. Rev. Lett.* **113**, 046802 (2014).
- [16] P. Titum, N. H. Lindner, M. C. Rechtsman, and G. Refael, “Disorder-induced floquet topological insulators”, *Phys. Rev. Lett.* **114**, 056801 (2015).
- [17] C. Liu, W. Gao, B. Yang, and S. Zhang, “Disorder-induced topological state transition in photonic metamaterials”, *Phys. Rev. Lett.* **119**, 183901 (2017).
- [18] S. Stützer, Y. Plotnik, Y. Lumer, P. Titum, N. H. Lindner, M. Segev, M. C. Rechtsman, and A. Szameit, “Photonic topological anderson insulators”, *Nature* **560**, 461 (2018).
- [19] E. J. Meier, F. A. An, A. Dauphin, M. Maffei, P. Massignan, T. L. Hughes, and B. Gadway, “Observation of the topological anderson insulator in disordered atomic wires”, *Science* **362**, 929 (2018).
- [20] R. Chen, D.-H. Xu, and B. Zhou, “Topological anderson insulator phase in a quasicrystal lattice”, *Phys. Rev. B* **100**, 115311 (2019).
- [21] C.-A. Li, B. Fu, Z.-A. Hu, J. Li, and S.-Q. Shen, “Topological phase transitions in disordered electric quadrupole insulators”, *Phys. Rev. Lett.* **125**, 166801 (2020).
- [22] G.-G. Liu, Y. Yang, X. Ren, H. Xue, X. Lin, Y.-H. Hu, *et al.*, “Topological anderson insulator in disordered photonic crystals”, *Phys. Rev. Lett.* **125**, 133603 (2020).
- [23] D.-W. Zhang, L.-Z. Tang, L.-J. Lang, H. Yan, and S.-L. Zhu, “Non-hermitian topological anderson insulators”, *Sci. China Phys., Mech. & Astron.* **63**, 267062 (2020).
- [24] Y.-B. Yang, K. Li, L.-M. Duan, and Y. Xu, “Higher-order topological anderson insulators”, *Phys. Rev. B* **103**, 085408 (2021).
- [25] X. Cui, R.-Y. Zhang, Z.-Q. Zhang, and C. T. Chan, “Photonic z_2 topological anderson insulators”, *Phys. Rev.*

- Lett. **129**, 043902 (2022).
- [26] X. Cheng, T. Qu, L. Xiao, S. Jia, J. Chen, and L. Zhang, “Topological anderson amorphous insulator”, Phys. Rev. B **108**, L081110 (2023).
- [27] N. Sobrosa, M. Gonçalves, and E. V. Castro, “Instability of quadratic band crossing systems to topological anderson insulating phases”, Phys. Rev. B **109**, 184206 (2024).
- [28] M. Ren, Y. Yu, B. Wu, X. Qi, Y. Wang, X. Yao, *et al.*, “Realization of gapped and ungapped photonic topological anderson insulators”, Phys. Rev. Lett. **132**, 066602 (2024).
- [29] B. I. Halperin, P. A. Lee, and N. Read, “Theory of the half-filled landau level”, Phys. Rev. B **47**, 7312 (1993).
- [30] T. Sugiyama and N. Nagaosa, “Localization in a random magnetic field in 2d”, Phys. Rev. Lett. **70**, 1980 (1993).
- [31] Y. Avishai, Y. Hatsugai, and M. Kohmoto, “Localization problem of a two-dimensional lattice in a random magnetic field”, Phys. Rev. B **47**, 9561 (1993).
- [32] A. G. Aronov, A. D. Mirlin, and P. Wölfle, “Localization of charged quantum particles in a static random magnetic field”, Phys. Rev. B **49**, 16609 (1994).
- [33] D. N. Sheng and Z. Y. Weng, “Delocalization of electrons in a random magnetic field”, Phys. Rev. Lett. **75**, 2388 (1995).
- [34] X. C. Xie, X. R. Wang, and D. Z. Liu, “Kosterlitz-thouless-type metal-insulator transition of a 2d electron gas in a random magnetic field”, Phys. Rev. Lett. **80**, 3563 (1998).
- [35] A. Furusaki, “Anderson localization due to a random magnetic field in two dimensions”, Phys. Rev. Lett. **82**, 604 (1999).
- [36] A. Altland and B. Simons, “Field theory of the random flux model”, Nucl. Phys. B **562**, 445 (1999).
- [37] D. Taras-Semchuk and K. B. Efetov, “Antilocalization in a 2d electron gas in a random magnetic field”, Phys. Rev. Lett. **85**, 1060 (2000).
- [38] V. Z. Cerovski, “Critical exponent of the random flux model on an infinite two-dimensional square lattice and anomalous critical states”, Phys. Rev. B **64**, 161101 (2001).
- [39] P. Markoš and L. Schweitzer, “Critical conductance of two-dimensional chiral systems with random magnetic flux”, Phys. Rev. B **76**, 115318 (2007).
- [40] J. Major, M. Płodzień, O. Dutta, and J. Zakrzewski, “Synthetic random flux model in a periodically driven optical lattice”, Phys. Rev. A **96**, 033620 (2017).
- [41] C.-A. Li, S.-B. Zhang, J. C. Budich, and B. Trauzettel, “Transition from metal to higher-order topological insulator driven by random flux”, Phys. Rev. B **106**, L081410 (2022).
- [42] X. Wu, F. Yang, S. Yang, K. Mølmer, T. Pohl, M. K. Tey, and L. You, “Manipulating synthetic gauge fluxes via multicolor dressing of rydberg-atom arrays”, Phys. Rev. Res. **4**, L032046 (2022).
- [43] T. Mizoguchi and Y. Hatsugai, “Molecular-orbital representation with random $u(1)$ variables”, Phys. Rev. B **107**, 094201 (2023).
- [44] Z. Zhuang, “Transport in honeycomb lattice with random π fluxes: Implications for low-temperature thermal transport in kitaev spin liquids”, Phys. Rev. B **108**, 134203 (2023).
- [45] F.-J. Wang, Z.-Y. Xiao, R. Queiroz, B. A. Bernevig, A. Stern, and Z.-D. Song, “Anderson critical metal phase in trivial states protected by average magnetic crystalline symmetry”, Nat. Commun. **15**, 3069 (2024).
- [46] A. Altland and M. R. Zirnbauer, “Nonstandard symmetry classes in mesoscopic normal-superconducting hybrid structures”, Phys. Rev. B **55**, 1142 (1997).
- [47] X.-L. Qi, Y.-S. Wu, and S.-C. Zhang, “Topological quantization of the spin hall effect in two-dimensional paramagnetic semiconductors”, Phys. Rev. B **74**, 085308 (2006).
- [48] Y. Yoshimura, K.-I. Imura, T. Fukui, and Y. Hatsugai, “Characterizing weak topological properties: Berry phase point of view”, Phys. Rev. B **90**, 155443 (2014).
- [49] L. Fu and C. L. Kane, “Topological insulators with inversion symmetry”, Phys. Rev. B **76**, 045302 (2007).
- [50] T. L. Hughes, E. Prodan, and B. A. Bernevig, “Inversion-symmetric topological insulators”, Phys. Rev. B **83**, 245132 (2011).
- [51] See Supplemental Material at [URL to be added by publisher] for details of (Sec. S1) the properties of anisotropic Wilson-Dirac model; (Sec. S2) effective band structures from averaged Green’s function; (Sec. S3) effective medium theory of random-flux induced topological phase transitions; (Sec. S4) phase diagram under different parameter settings; (Sec. S5) critical features at phase transition points from CIs to NIs; (Sec. S6) local density of states for different phases under random flux; and (Sec. S7) robustness of topological random-flux insulators against on-site potential disorders, which includes Refs. [10, 48, 50].
- [52] In the following, we take the gauge choice $\mathbf{A}(\mathbf{r}) = (-B(\mathbf{r})y, 0, 0)$. The hopping terms are modified as $t_{\langle mn \rangle} \rightarrow t_{\langle mn \rangle} \exp[i\theta_{mn}]$, where the $U(1)$ phase factors are $\theta_{mn} = \int_m^n \mathbf{A}(\mathbf{r}) \cdot d\mathbf{r}$ and $t_{\langle mn \rangle}$ indicates the nearest-neighbor hopping between sites m and n . Note that different gauge choice does not change the results.
- [53] D. Toniolo, “On the bott index of unitary matrices on a finite torus”, Letters in Mathematical Physics **112**, 126 (2022).
- [54] T. A. Loring and M. B. Hastings, “Disordered topological insulators via c^* -algebras”, Eur. Phys. Lett. **92**, 67004 (2010).
- [55] The projected position matrices take the form $P e^{i2\pi\hat{x}(\hat{y})/L_{x/y}} P \sim \begin{pmatrix} 0 & 0 \\ 0 & \tilde{U}_{x/y} \end{pmatrix}$.
- [56] S. Datta, *Electronic Transport in Mesoscopic Systems* (Cambridge University Press, Cambridge, 1995).
- [57] The conductance G can be evaluated as $G = \frac{e^2}{h} \text{Tr}[\Gamma_L G^r \Gamma_R G^a]$, where $G^{r,a}$ are the retarded and advanced Green’s functions, respectively, and $\Gamma_{L,R}$ are the line-width functions coupling two terminals to the central region of interest.
- [58] A. MacKinnon and B. Kramer, “The scaling theory of electrons in disordered solids: Additional numerical results”, Z. Phys. B **53**, 1 (1983).
- [59] Notably, $D_{\alpha\beta}(\mathbf{q})$ exhibits strong singularity in the forward direction ($\mathbf{q} = 0$) which leads to infrared divergences in self-energy calculations, necessitating a regulation due to the electron-field coupling, as shown in the SM [51].
- [60] Prior to impurity averaging, two momentum labels are required for the Green’s function G^r in a disordered system, due to the breakdown of translation symmetry.
- [61] A. Chen, H. Brand, T. Helbig, T. Hofmann, S. Imhof, A. Fritzsche, *et al.*, “Hyperbolic matter in electrical cir-

- cuits with tunable complex phases”, Nat. Commun. **14**, 622 (2023).
- [62] M. Schmidt, S. Kessler, V. Peano, O. Painter, and F. Marquardt, “Optomechanical creation of magnetic fields for photons on a lattice”, *Optica* **2**, 635 (2015).
- [63] M. Aidelsburger, M. Atala, M. Lohse, J. T. Barreiro,

- B. Paredes, and I. Bloch, “Realization of the hofstadter hamiltonian with ultracold atoms in optical lattices”, *Phys. Rev. Lett.* **111**, 185301 (2013).
- [64] G. Jotzu, M. Messer, R. Desbuquois, M. Lebrat, T. Uehlinger, D. Greif, and T. Esslinger, “Experimental realization of the topological haldane model with ultracold fermions”, *Nature* **515**, 237 (2014).

Supplemental materials of “Random-Flux-Induced Topological Phase Transitions and Chern Insulators”

Appendix S1: Properties of the anisotropic Wilson-Dirac model

In this section, we present the band structure, Chern number, and weak topology of the anisotropic Wilson-Dirac (AWD) model. The Bloch Hamiltonian for AWD model reads [see Eq. (1) of the main text]

$$H(\mathbf{k}) = \mathbf{d}(\mathbf{k}) \cdot \boldsymbol{\sigma}, \quad (\text{S1.1})$$

where

$$\mathbf{d}(\mathbf{k}) \equiv (v_x \sin k_x, v_y \sin k_y, m + \sum_{i=x,y} b_i \cos k_i), \quad (\text{S1.2})$$

and $\boldsymbol{\sigma} = (\sigma_x, \sigma_y, \sigma_z)$ represents the Pauli matrices. The vector $\mathbf{k} \equiv (k_x, k_y)$ is the Bloch wave vector. Here, m is the mass term, and b_i and v_i are model parameters. The two energy bands are

$$E_{\pm}(\mathbf{k}) = \pm |\mathbf{d}(\mathbf{k})| = \pm \sqrt{(m + \sum_i b_i \cos k_i)^2 + \sum_i v_i^2 \sin^2 k_i} \quad (\text{S1.3})$$

with corresponding eigenstates

$$\psi_+(\mathbf{k}) = \begin{pmatrix} \cos \frac{\theta(\mathbf{k})}{2} e^{-i\varphi(\mathbf{k})} \\ \sin \frac{\theta(\mathbf{k})}{2} \end{pmatrix}, \quad \psi_-(\mathbf{k}) = \begin{pmatrix} \sin \frac{\theta(\mathbf{k})}{2} e^{-i\varphi(\mathbf{k})} \\ -\cos \frac{\theta(\mathbf{k})}{2} \end{pmatrix}, \quad (\text{S1.4})$$

where $\theta(\mathbf{k}) \equiv \arccos \frac{d_z(\mathbf{k})}{|\mathbf{d}(\mathbf{k})|}$, and $\varphi(\mathbf{k}) \equiv \arctan \frac{d_y(\mathbf{k})}{d_x(\mathbf{k})}$.

The Chern number at half-filling can be calculated as

$$\begin{aligned} C &= \int_{BZ} \frac{d\mathbf{k}}{4\pi |\mathbf{d}(\mathbf{k})|^3} \mathbf{d}(\mathbf{k}) \cdot \partial_{k_x} \mathbf{d}(\mathbf{k}) \times \partial_{k_y} \mathbf{d}(\mathbf{k}) \\ &= \int_0^{2\pi} \int_0^{2\pi} \frac{v_x v_y [b_x \cos k_y + b_y \cos k_x + m \cos k_x \cos k_y]}{4\pi |\mathbf{d}(\mathbf{k})|^3} dk_x dk_y. \end{aligned} \quad (\text{S1.5})$$

For simplicity, we define $b_{\pm} \equiv |b_x \pm b_y|$ and assume $b_+ > b_-$ and $v_x v_y > 0$. The Chern number takes

$$C(m) = \begin{cases} 0, & |m| > b_+; \\ +1, & -b_+ < m < -b_-; \\ 0, & |m| < b_-; \\ -1, & b_- < m < b_+. \end{cases} \quad (\text{S1.6})$$

The clean phase diagram is shown in Fig. 1(a) of the main text, which is identical to the calculation of Bott index. Note that the Chern number does not jump directly between $C = +1$ and $C = -1$, since the gap does not close at high symmetry points X and Y simultaneously as in the original model.

We note that the AWD model respects an inversion symmetry

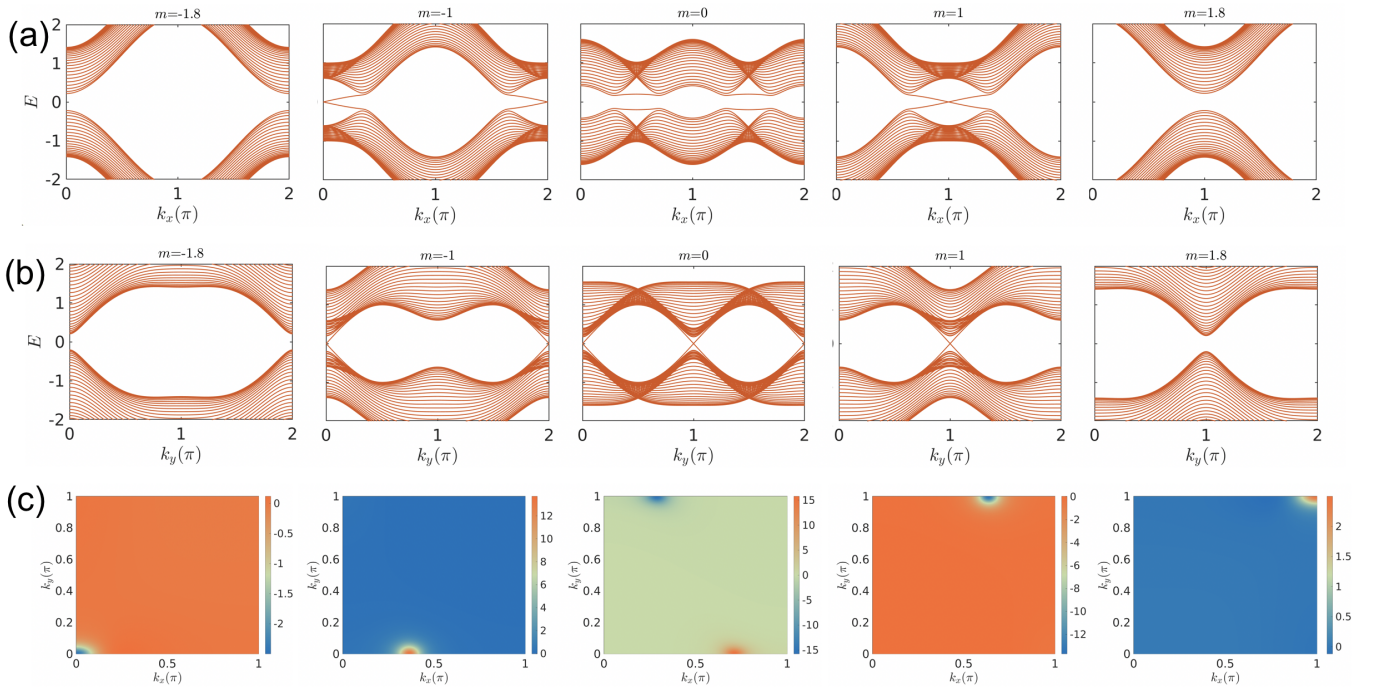


Figure S1. (a) Energy spectra of a ribbon geometry along x direction under open boundary conditions for different parameter m . (b) The same as (a) but along y direction. (c) The Berry curvature $F(k_x, k_y)$ plotted corresponding the parameter settings in (a) and (b). Other parameters are: $b_x = 1, b_y = 0.6, v_x = 0.2$, and $v_y = 1$.

$$\mathcal{P}H(\mathbf{k})\mathcal{P}^{-1} = H(-\mathbf{k}), \quad (\text{S1.7})$$

where $\mathcal{P} = \sigma_z$. In this case, the topology of the system can be fully determined by examining four high-symmetry points (HSPs). The Chern number is directly connected to the parity of occupied bands at these HSPs through the relation [50]

$$(-1)^C = \prod_{j=1}^4 \xi_j(K_j), \quad (\text{S1.8})$$

where $K_j \in \{K_1 = \Gamma(0, 0), K_2 = X(\pi, 0), K_3 = M(\pi, \pi), K_4 = Y(0, \pi)\}$, and $\xi_j = \pm 1$ is the parity value defined by $\mathcal{P}\psi_-(K_j) = \xi_j\psi_-(K_j)$. At these HSPs, the parity is related to the effective mass by

$$\xi_j = -\text{sgn}(\tilde{m}_{K_j}). \quad (\text{S1.9})$$

The gap-closing transition flips the sign of the effective mass term at HSPs, which in turn changes the parity values and thus changes the Chern number.

The nonzero Chern number indicates the existence of chiral edge modes at open boundaries. In Figs. S1(a) and S1(b), we show the energy spectra along x and y directions, respectively, corresponding to five different phase regions with increasing the parameter m in Fig. 1(a) of the main text. Let us focus on the case with $m = 0$. Here, the Chern number is $C = 0$ since the Berry curvature cancels out across the Brillouin zone [Fig. S1(c)]. However, we observe two pairs of Dirac edge modes along y direction (at $k_y^* = 0, \pi$) but no Dirac edge modes along x direction. This phase is identified as a weak topological insulator (WTI). Therefore, the Chern number $C = 0$ cannot distinguish between the normal insulator (NI) and WTI.

To address this, we introduce two weak Z_2 indices, (ν_x, ν_y) , based on parity configurations at HSPs. These indices complement the strong index $C = 0$ and identify the WTI. In a WTI, the parity configuration ξ_j at HSPs takes two positive and two negative values, while for a NI, parity values ξ_j at four HSPs are all positive or all negative. The WTI is essentially topological trivial in 2D because it can be fully characterized by topological indices defined in 1D. To illustrate this, let us reduce the dimensionality to 1D by setting $k_y^* = 0$ or π , leading to the following Hamiltonian

$$H(k_x, k_y^* = 0/\pi) = (m \pm b_y + b_x \cos k_x)\sigma_z + v_x \sin(k_x)\sigma_x. \quad (\text{S1.10})$$

By applying a unitary transformation with $U(\theta) = \exp(-i\frac{\pi}{4}\sigma_z)\exp(-i\frac{\pi}{4}\sigma_x)$, the Hamiltonian transforms to

$$\tilde{H}(k_x, k_y^*) = (m \pm b_y + b_x \cos k_x)\sigma_x + v_x \sin(k_x)\sigma_y. \quad (\text{S1.11})$$

This 1D Hamiltonian respects inversion symmetry as well as chiral symmetry. Its topology is characterized by a quantized polarization $p_x = 0/\frac{1}{2}$ (or equivalently winding number 0/1). With the help of inversion symmetry, we obtain [50]

$$\xi_1 \xi_2 = e^{i2\pi p_x (k_y^*=0)}, \quad (\text{S1.12})$$

$$\xi_3 \xi_4 = e^{i2\pi p_x (k_y^*=\pi)}. \quad (\text{S1.13})$$

Due to the constraint $\xi_1 \xi_2 = \xi_3 \xi_4$, we can define the weak index ν_x as

$$(-1)^{\nu_x} = \xi_1 \xi_2. \quad (\text{S1.14})$$

To have $\nu_x = 1$, it requires

$$|m + b_y| < b_x \cap |m - b_y| < b_x. \quad (\text{S1.15})$$

For our parameter setting in the main text, it gives $|m| < b_-$, which is consistent with the phase diagram. Similarly, the weak index ν_y can be defined as

$$(-1)^{\nu_y} = \xi_1 \xi_4. \quad (\text{S1.16})$$

For $\nu_y = 1$, it requires

$$|m + b_x| < b_y \cap |m - b_x| < b_y. \quad (\text{S1.17})$$

For the parameter setting in the main text, it gives $\{m\} = \emptyset$, meaning no solutions for the $\nu_y = 1$.

For the NI and WTI with $C = 0$, the model distinguishes three distinct phases by $(C = 0; \nu_x \nu_y) = (0; 00), (0; 01),$ and $(0; 10)$, respectively. The NI phase has $(C; \nu_x \nu_y) = (0; 00)$. The WTI phases with $\nu_{x,y} \neq 0$ indicate the presence of two pairs of Dirac edge modes when the x/y direction is subjected to an open boundary condition [see Figs. S1(a) and S1(b)]. From the constraints in Eqs. (S1.15) and (S1.17), it is impossible to have nonzero ν_x and ν_y at the same time for the $C = 0$ case.

Appendix S2: Effective band structures from averaged Green's function

In this section, we present the effective band structures obtained from averaged Green's function and their corresponding Berry curvatures. We average the Green's function over a large enough number of random configurations, such that the translation symmetry can be effectively restored and an effective Hamiltonian can be obtained.

The random flux averaged Green's function is given by $G_{\text{avg}}^r(\mathbf{r} - \mathbf{r}', E) = \langle G^r(\mathbf{r}, \mathbf{r}', E) \rangle$, where $\langle \dots \rangle$ indicates the disorder average. By Fourier transforming the averaged Green's function, we obtain $G^r(\mathbf{k}, E) = \sum_{\mathbf{r}} G_{\text{avg}}^r(\mathbf{r}, E) e^{i\mathbf{k} \cdot \mathbf{r}}$. From this, the effective Hamiltonian is derived as

$$H_{\text{eff},G}(\mathbf{k}) = -[G^r(\mathbf{k}, E = 0)]^{-1}. \quad (\text{S2.1})$$

The Berry curvatures can be calculated by the lattice gauge theory method described in Ref. [48]. First, we solve the eigenvalue problem for the effective Hamiltonian $H_{\text{eff},G}(\mathbf{k})$ on a discretized Brillouin zone mesh, $H_{\text{eff},G}(\mathbf{k}_j)|\varphi_n(\mathbf{k}_j)\rangle = \epsilon_n|\varphi_n(\mathbf{k}_j)\rangle$, where the momentum points are $\mathbf{k}_j \equiv (j_x e_{k_x}, j_y e_{k_y})$ with $e_{k_x} = \frac{2\pi}{N_x}$ and $e_{k_y} = \frac{2\pi}{N_y}$. The $U(1)$ link for the occupied band is defined as $M_{\alpha=x,y}(\mathbf{k}_j) \equiv |\det U_{\alpha}(\mathbf{k}_j)|^{-1} \det U_{\alpha}(\mathbf{k}_j)$ with the matrix $U_{\alpha}(\mathbf{k}_j) = \langle \varphi(\mathbf{k}_j) | \varphi(\mathbf{k}_j + \hat{e}_{\alpha}) \rangle$. This link variables are well-defined except at singular points with $\det U_{\alpha}(\mathbf{k}_j) = 0$. Using these link variables, we obtain a lattice field strength as

$$F(\mathbf{k}_j) \equiv \ln [M_x(\mathbf{k}_j) M_y(\mathbf{k}_j + \hat{e}_x) M_x^{-1}(\mathbf{k}_j + \hat{e}_y) M_y^{-1}(\mathbf{k}_j)]. \quad (\text{S2.2})$$

In Figs. S2(a1), S2(b1), and S2(c1), we show the band structures of the effective Hamiltonian $H_{\text{eff},G}(\mathbf{k})$ for different random flux strengths, $U_d = 0.1\pi, 1.0\pi,$ and 1.9π , respectively. The band structure evolves as changing U_d . Figures S2(a2), S2(b2), and S2(c2) are the corresponding Berry curvatures $F(k_x, k_y)$. For small random flux strength $U_d = 0.1\pi$, the Berry curvature features both peak and dip, which cancel out, resulting in a Chern number $C = 0$. It is still in the WTI with $(C; \nu_x \nu_y) = (0; 10)$. At an intermediate random flux strength $U_d = 1.0\pi$, the system is driven to a topological random flux insulator with $C = 1$. The corresponding Berry curvature show peaks only [Fig. S2(b2)]. As increasing U_d further to $U_d = 1.9\pi$, the Berry curvature gives zero Chern number in the phase $(C; \nu_x \nu_y) = (0; 01)$.

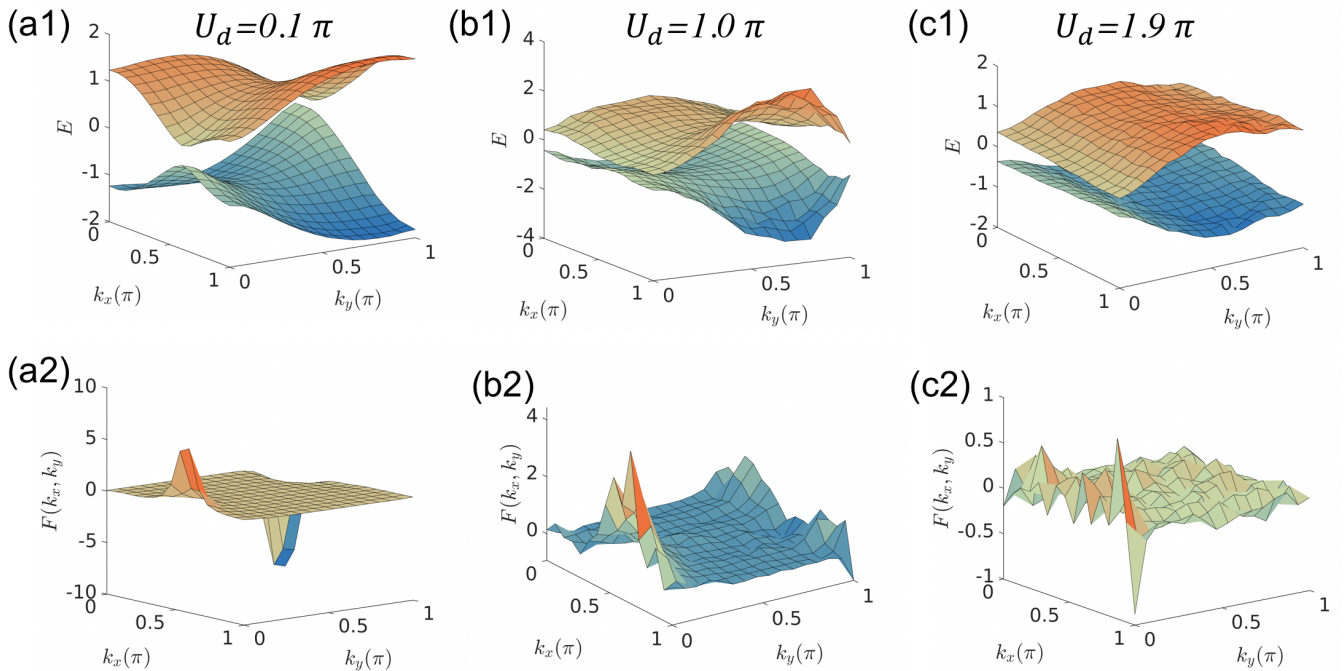


Figure S2. Effective bands structures [upper panel] and their corresponding Berry curvatures [lower panel] for representative random flux strength $U_d = 0.1\pi, 1.0\pi$, and 1.9π , respectively. Other parameters are: $m = -0.3, b_x = 1, b_y = 0.6, v_x = 0.2$, and $v_y = 1$.

Appendix S3: Effective medium theory of random-flux-induced topological phase transitions

In this section, we present the details for the effective medium theory that accounts for random-flux-induced topological phase transitions. The random flux is connected to a random magnetic field as $\phi(\mathbf{r}) = B(\mathbf{r})$. Therefore, the random magnetic field is then uniformly distributed in the interval $[-U_d/2, U_d/2]$, where U_d represents the random flux strength. The disorder averages of products of two random magnetic fields are given by

$$\langle B(\mathbf{q})B(-\mathbf{q}) \rangle = \frac{U_d^2}{12} \delta_{\mathbf{q}+\mathbf{q}',0}, \quad (\text{S3.1})$$

where $B(\mathbf{q})$ is the Fourier transform of the random magnetic field defined as $B(\mathbf{q}) = \int d\mathbf{r} e^{-i\mathbf{q}\cdot\mathbf{r}} B(\mathbf{r})$. The corresponding vector potential $A_\alpha(\mathbf{q})$, which generates the fluctuating magnetic field, can be expressed as

$$A_\alpha(\mathbf{q}) = \frac{i\epsilon_{\alpha\beta} q_\beta}{q^2} B(\mathbf{q}), \quad (\text{S3.2})$$

where $\epsilon_{\alpha\beta}$ is the Levi-Civita symbol in two dimensions, and α, β range over x, y . The correlations between vector potentials are given by

$$\langle A_\alpha(\mathbf{q})A_\beta(\mathbf{q}') \rangle = \mathcal{V} \frac{U_d^2}{12} \frac{\delta_{\alpha\beta} - \hat{q}_\alpha \hat{q}_\beta}{|\mathbf{q}|^2} \delta_{\mathbf{q}+\mathbf{q}',0}, \quad (\text{S3.3})$$

where \mathcal{V} is the volume. For convenience, we define the correlator

$$D_{\alpha\beta}(\mathbf{q}) \equiv \frac{U_d^2}{12} \frac{\delta_{\alpha\beta} - \hat{q}_\alpha \hat{q}_\beta}{|\mathbf{q}|^2}, \quad (\text{S3.4})$$

where the term $(\delta_{\alpha\beta} - \hat{q}_\alpha \hat{q}_\beta)$ accounts for the transverse nature of the vector potential with $\hat{q}_\alpha \equiv q_\alpha/|\mathbf{q}|$.

In the presence of random flux, the minimally coupled Hamiltonian \hat{H} is transformed to \hat{H}_A given by

$$\hat{H}_A = \sum_{\mathbf{r}} \hat{\psi}_{\mathbf{r}}^\dagger \mathbf{d} [-i\partial_{\mathbf{r}} + e\mathbf{A}(\mathbf{r})] \cdot \hat{\sigma} \hat{\psi}_{\mathbf{r}}. \quad (\text{S3.5})$$

We expand the full Hamiltonian into two components

$$\hat{H}_A = \hat{H}_0 + \hat{V}[\mathbf{A}(\mathbf{r})], \quad (\text{S3.6})$$

where \hat{H}_0 is the Hamiltonian in the clean limit and $\hat{V}[\mathbf{A}(\mathbf{r})]$ is the perturbed potential that can be expressed as $\hat{V} = \sum_{\mathbf{k}, \mathbf{k}'} \psi_{\mathbf{k}}^\dagger V(\mathbf{k}, \mathbf{k}') \psi_{\mathbf{k}'}$. Here, $V(\mathbf{k}, \mathbf{k}')$ includes interaction terms of all orders

$$V(\mathbf{k}, \mathbf{k}') = \sum_{n=1}^{\infty} V_n(\mathbf{k}, \mathbf{k}'), \quad (\text{S3.7})$$

where $V_n(\mathbf{k}, \mathbf{k}')$ accounts for the n -th order interaction with explicit form

$$V_n(\mathbf{k}, \mathbf{k}') = \frac{1}{n!} \sum_{\mathbf{q}_1, \mathbf{q}_2, \dots, \mathbf{q}_{n-1}} \Gamma_{\alpha}(\mathbf{k}, \mathbf{k}') A_{\alpha_1}(-\mathbf{q}_1) A_{\alpha_2}(-\mathbf{q}_2) \cdots A_{\alpha_n}(\mathbf{k} - \mathbf{k}' + \mathbf{q}_n), \quad (\text{S3.8})$$

where $\mathbf{q}_n \equiv \sum_{i=1}^{n-1} \mathbf{q}_i$, $\alpha \equiv \{\alpha_1, \alpha_2, \dots, \alpha_n\}$ and $\Gamma_{\alpha}(\mathbf{k}, \mathbf{k}') \equiv \frac{1}{2}[J_{\alpha}(\mathbf{k}) + J_{\alpha}(\mathbf{k}')]$ is the n -th order vertex. $J_{\alpha}(\mathbf{k})$ is the trapezoidal current operator defined as

$$J_{\alpha}(\mathbf{k}) \equiv \frac{\partial_n H(\mathbf{k})}{\partial k_{\alpha_1} \partial k_{\alpha_2} \cdots \partial k_{\alpha_n}}. \quad (\text{S3.9})$$

The random flux averaging of the perturbative component $\hat{V}[A(\mathbf{r})]$ involves multiple orders of the vector potential, which are taken into account by introducing the generating functional

$$\begin{aligned} \mathcal{G}[\eta, \bar{\eta}] &= \mathcal{Z}^{-1} \int D[A] e^{-\frac{1}{2} \int d\mathbf{r} \int d\mathbf{r}' A_{\alpha}(\mathbf{r}) D_{\alpha\beta}^{-1}(\mathbf{r}, \mathbf{r}') A_{\beta}(\mathbf{r}') + \int d\mathbf{r} \eta_{\alpha}(\mathbf{r}) A_{\alpha}(\mathbf{r})} \\ &= e^{\int d\mathbf{r} \int d\mathbf{r}' \eta_{\alpha}(\mathbf{r}) D_{\alpha\beta}(\mathbf{r} - \mathbf{r}') \eta_{\beta}(\mathbf{r}')}, \end{aligned} \quad (\text{S3.10})$$

where $\eta_{\alpha}(\mathbf{r})$ is an arbitrary real field, and $\mathcal{Z} = \int D[A] e^{-\frac{1}{2} \int d\mathbf{r} \int d\mathbf{r}' A_{\alpha}(\mathbf{r}) D_{\alpha\beta}^{-1}(\mathbf{r}, \mathbf{r}') A_{\beta}(\mathbf{r}')}$ is the multidimensional Gaussian integral. Differentiating the functional integral twice with respect to η according to $\frac{\partial^2 \mathcal{G}[\eta, \bar{\eta}]}{\partial \eta_{\alpha}(\mathbf{r}) \partial \eta_{\beta}(\mathbf{r}')}|_{\eta, \bar{\eta}=0}$ yields the averaged products of two vector potentials

$$\langle A_{\alpha}(\mathbf{r}) A_{\beta}(\mathbf{r}') \rangle = D_{\alpha\beta}(\mathbf{r} - \mathbf{r}'), \quad (\text{S3.11})$$

which is exactly the Fourier transformation of the Eq. (S3.3): $D_{\alpha\beta}(\mathbf{r} - \mathbf{r}') = \frac{1}{\mathcal{V}} \sum_{\mathbf{q}} e^{i\mathbf{q} \cdot (\mathbf{r} - \mathbf{r}')} D_{\alpha\beta}(\mathbf{q})$. For higher-order averages involving $2n$ vector potentials, differentiation of the generating function $2n$ times results in

$$\langle A_{\alpha_1}(\mathbf{r}_1) A_{\alpha_2}(\mathbf{r}_2) \cdots A_{\alpha_{2n}}(\mathbf{r}_{2n}) \rangle = \sum_{\text{pairs of } \{i_1, \dots, i_{2n}\}} D_{\alpha_{i_1} \alpha_{i_2}}(\mathbf{r}_{\alpha_{i_1}} - \mathbf{r}_{\alpha_{i_2}}) \times \cdots \times D_{\alpha_{i_{2n-1}} \alpha_{i_{2n}}}(\mathbf{r}_{\alpha_{i_{2n-1}}} - \mathbf{r}_{\alpha_{i_{2n}}}), \quad (\text{S3.12})$$

which is given by all possible pairings that can be formed from the $2n$ components of $A(\mathbf{r})$.

We now evaluate the random flux averaging of the perturbation part as defined in Eq. (S3.7)

$$\langle V(\mathbf{k}, \mathbf{k}') \rangle = \sum_{n=1}^{\infty} \frac{1}{n! \mathcal{V}^n} \sum_{\mathbf{q}_1, \mathbf{q}_2, \dots, \mathbf{q}_{n-1}} \Gamma_{\alpha}(\mathbf{k}, \mathbf{k}') \langle A_{\alpha_1}(-\mathbf{q}_1) A_{\alpha_2}(-\mathbf{q}_2) \cdots A_{\alpha_n}(\mathbf{k} - \mathbf{k}' + \mathbf{q}_n) \rangle. \quad (\text{S3.13})$$

According to Eq. (S3.12), only even orders of A survive after disorder averaging (see Fig. 4(a) in the main text). Given that $V(\mathbf{k}, \mathbf{k}')$ contains all order of vector potential, the disorder average of the first order $\langle V(\mathbf{k}, \mathbf{k}') \rangle$ is nonzero, in stark contrast to that of on-site potential disorder. Using the relations $\frac{1}{\mathcal{V}} \sum_{\mathbf{q}} D_{\alpha\beta}(\mathbf{q}) = \delta_{\alpha\beta} \frac{1}{\mathcal{V}} \sum_{\mathbf{q}} D_{\alpha\alpha}(\mathbf{q})$ and $\Gamma_{[\alpha \cdots \alpha]_{2n}}(\mathbf{k}, \mathbf{k}') = (-1)^{n+1} J_{\alpha\alpha}(\mathbf{k})$ for the AWD model, it can be further recast in a closed form as

$$\langle V(\mathbf{k}, \mathbf{k}') \rangle = J_{\alpha\alpha}(\mathbf{k}) [1 - e^{-\frac{1}{2\mathcal{V}} \sum_{\mathbf{q}} D_{\alpha\alpha}(\mathbf{q})}] \delta_{\mathbf{k}, \mathbf{k}'}. \quad (\text{S3.14})$$

We then evaluate the random flux averaging over the product of two perturbative potentials, which involves considering all combinations of two perturbative parts

$$\begin{aligned}
\langle V(\mathbf{k}, \mathbf{k}_1) \otimes V(\mathbf{k}_1, \mathbf{k}') \rangle &= \frac{1}{\mathcal{V}^2} \Gamma_\alpha(\mathbf{k}, \mathbf{k}_1) \otimes \Gamma_{\alpha'}(\mathbf{k}_1, \mathbf{k}') \langle A_\alpha(\mathbf{k} - \mathbf{k}_1) A_{\alpha'}(\mathbf{k}_1 - \mathbf{k}') \rangle \\
&+ \frac{1}{3! \mathcal{V}^4} \Gamma_\alpha(\mathbf{k}, \mathbf{k}_1) \otimes \Gamma_{\alpha'_1 \alpha'_2 \alpha'_3}(\mathbf{k}_1, \mathbf{k}') \sum_{\mathbf{q}'_1, \mathbf{q}'_2} \langle A_\alpha(\mathbf{k} - \mathbf{k}_1) A_{\alpha'_1}(-\mathbf{q}'_1) A_{\alpha'_2}(-\mathbf{q}'_2) A_{\alpha'_3}(\mathbf{k}_1 - \mathbf{k}' + \mathbf{q}'_1 + \mathbf{q}'_2) \rangle \\
&+ \frac{1}{3! \mathcal{V}^4} \Gamma_{\alpha_1 \alpha_2 \alpha_3}(\mathbf{k}, \mathbf{k}_1) \otimes \Gamma_{\alpha'}(\mathbf{k}_1, \mathbf{k}') \sum_{\mathbf{q}_1, \mathbf{q}_2} \langle A_{\alpha_1}(-\mathbf{q}_1) A_{\alpha_2}(-\mathbf{q}_2) A_{\alpha_3}(\mathbf{k}_1 - \mathbf{k} + \mathbf{q}_1 + \mathbf{q}_2) A_{\alpha'}(\mathbf{k}_1 - \mathbf{k}') \rangle \\
&+ \frac{1}{2! \mathcal{V}^2} \Gamma_{\alpha_1 \alpha_2}(\mathbf{k}, \mathbf{k}_1) \otimes \Gamma_{\alpha'_1 \alpha'_2}(\mathbf{k}_1, \mathbf{k}') \sum_{\mathbf{q}'_1, \mathbf{q}'_2} \langle A_{\alpha_1}(-\mathbf{q}_1) A_{\alpha_2}(\mathbf{k} - \mathbf{k}_1 + \mathbf{q}_1) A_{\alpha'_1}(-\mathbf{q}'_1) A_{\alpha'_2}(\mathbf{k}_1 - \mathbf{k}' + \mathbf{q}'_1) \rangle \\
&+ \dots
\end{aligned} \tag{S3.15}$$

By truncating to the lowest order of nonvanishing terms, we approximate:

$$\langle V(\mathbf{k}, \mathbf{k}_1) \otimes V(\mathbf{k}_1, \mathbf{k}') \rangle \simeq \frac{1}{\mathcal{V}} \Gamma_\alpha(\mathbf{k}, \mathbf{k}_1) \otimes \Gamma_{\alpha'}(\mathbf{k}_1, \mathbf{k}') D_{\alpha\alpha'}(\mathbf{k} - \mathbf{k}') \delta_{\mathbf{k}\mathbf{k}'}. \tag{S3.16}$$

The Dyson equation in the presence of the perturbative component V can be expressed as follows

$$G^r(\mathbf{k}, \mathbf{k}', E) = \delta_{\mathbf{k}\mathbf{k}'} G_0^r(\mathbf{k}, E) + G_0^r(\mathbf{k}, E) \sum_{\mathbf{k}''} V(\mathbf{k}, \mathbf{k}'') G^r(\mathbf{k}'', \mathbf{k}', E). \tag{S3.17}$$

Prior to impurity averaging, the Green's function requires two momentum labels because translation symmetry is broken. To handle this, one can iteratively solve the right-hand side of the Dyson equation, averaging terms sequentially using Eqs. (S3.14) and (S3.16). This process helps to identify repeating structures that can be summed to an infinite order:

$$\begin{aligned}
\langle G^r(\mathbf{k}, \mathbf{k}', E) \rangle &= \delta_{\mathbf{k}\mathbf{k}'} G_0^r(\mathbf{k}, E) + G_0^r(\mathbf{k}, E) \langle V(\mathbf{k}, \mathbf{k}') \rangle G_0^r(\mathbf{k}', E) \\
&+ G_0^r(\mathbf{k}, E) \sum_{\mathbf{k}_1} \langle V(\mathbf{k}, \mathbf{k}_1) G_0^r(\mathbf{k}_1, E) V(\mathbf{k}_1, \mathbf{k}') \rangle G_0^r(\mathbf{k}', E) + \dots \\
&= \delta_{\mathbf{k}\mathbf{k}'} G_0^r(\mathbf{k}, E) \{ 1 + \langle V(\mathbf{k}, \mathbf{k}') \rangle G_0^r(\mathbf{k}', E) + \langle V(\mathbf{k}, \mathbf{k}) \rangle G_0^r(\mathbf{k}, E) \langle V(\mathbf{k}, \mathbf{k}) \rangle G_0^r(\mathbf{k}, E) \\
&+ \frac{1}{\mathcal{V}} \sum_{\mathbf{k}_1} D_{\alpha\alpha'}(\mathbf{k} - \mathbf{k}_1) \Gamma_\alpha(\mathbf{k}, \mathbf{k}_1) G_0^r(\mathbf{k}_1, E) \Gamma_{\alpha'}(\mathbf{k}_1, \mathbf{k}) G_0^r(\mathbf{k}, E) + \dots \}.
\end{aligned} \tag{S3.18}$$

After disorder averaging, translational symmetry is restored, as indicated by the presence of $\delta_{\mathbf{k}\mathbf{k}'}$. We can sum infinite subsets of diagrams, as depicted in Fig. 4 of the main text. The full Green's function is then expressed as:

$$G^r(\mathbf{k}, E) = [(G_0^r(\mathbf{k}, E))^{-1} - \Sigma(\mathbf{k}, E)] \tag{S3.19}$$

with the self-energy given by

$$\Sigma(\mathbf{k}, E) = \langle V(\mathbf{k}, \mathbf{k}) \rangle + \frac{1}{\mathcal{V}} \sum_{\mathbf{k}_1} D_{\alpha\alpha'}(\mathbf{k} - \mathbf{k}_1) \Gamma_\alpha(\mathbf{k}, \mathbf{k}_1) G^r(\mathbf{k}_1, E) \Gamma_{\alpha'}(\mathbf{k}_1, \mathbf{k}). \tag{S3.20}$$

The self-energy shows explicit dependence on wave vector \mathbf{k} , distinguishing it clearly from the on-site potential disorder case with a uniform mass renormalization [10]. After incorporating the self-energy $\Sigma(E, \mathbf{k})$, the preceding approach can quantitatively account for the modified phase diagram of the AWD model in the presence of random flux, as discussed in the main text.

Note that in the above calculations, the factor $D_{\alpha\beta}(\mathbf{k} - \mathbf{k}')$ exhibits a strong singularity in the forward direction $\mathbf{k} - \mathbf{k}'$ due to the extensive range of the vector potential fluctuations, despite the magnetic field fluctuations are short-ranged. To manage the infrared divergences in the self-energy calculations, we utilize the regulated correlator $\tilde{D}_{\alpha\beta}(\mathbf{k} - \mathbf{k}')$ instead. Drawing an analogy from the correction of the polarization tensor to the free gauge boson propagator in quantum electrodynamics (QED), we derive higher-order corrections to the impurity correlator for a

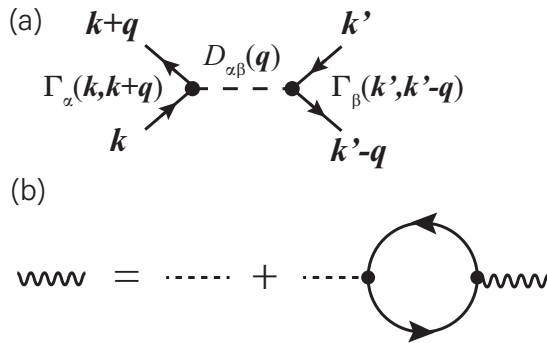


Figure S3. Effective four-fermion scatterings induced by the random flux. (b) Renormalization of the random gauge field correlator due to electron-field interactions. Wavy lines represent the dressed correlator for the vector potential. Dashed lines depict the bare correlator for the vector potential. Solid lines with arrows denote the electron propagators.

given system. This involves evaluating a diagram analogous to those used in QED as shown in Fig. S3 and solving a self-consistent equation for the renormalized impurity correlator:

$$\tilde{D}_{\alpha\beta}(\mathbf{q}) = D_{\alpha\beta}(\mathbf{q}) + D_{\alpha\gamma}(\mathbf{q})\Pi_{\gamma\delta}(\mathbf{q})\tilde{D}_{\alpha\beta}(\mathbf{q}), \quad (\text{S3.21})$$

where the polarization is given by

$$\Pi_{\gamma\delta}(\mathbf{q}) = \frac{1}{V} \sum_{\mathbf{k}} \text{Tr}[\Gamma_\gamma(\mathbf{k} + \mathbf{q}, \mathbf{k})G^r(\mathbf{k})\Gamma_\delta(\mathbf{k}, \mathbf{k} + \mathbf{q})G^r(\mathbf{k} + \mathbf{q})]. \quad (\text{S3.22})$$

It is revealed that the absolute values off-diagonal elements $\{|\Pi_{xy}|, |\Pi_{yx}|\}$ are much smaller than the diagonal elements $\{|\Pi_{xx}|, |\Pi_{yy}|\}$ with $\Pi_{xx}, \Pi_{yy} < 0$. Then, the polarization tensor can be approximated as $\Pi = \text{diag}\{\Pi_{xx}, \Pi_{yy}\}$. By substituting this result into Eq. (S3.21), we find

$$\tilde{D}_{\alpha\beta}(\mathbf{q}) \equiv \frac{U_d^2}{12} \frac{\delta_{\alpha\beta} - \hat{q}_\alpha \hat{q}_\beta}{|\mathbf{q}|^2 + \lambda_s^{-2}}, \quad (\text{S3.23})$$

where the screening length is defined as $\lambda_s = 1/\sqrt{-\frac{U_d^2}{12}(\Pi_{yy}\hat{q}_x^2 + \Pi_{xx}\hat{q}_y^2)}$. Consequently, the correlator of the random vector potential acquires effective screening due to the electron-gauge field interaction.

Appendix S4: Phase diagram under different parameter settings

In this section, we present the phase diagrams in terms of the Bott index under different parameter settings. Figure S4(a) illustrates the phase diagram for the case of on-site potential disorder, serving as a comparison with the random flux scenario. The on-site disorder takes a form of $V(\mathbf{r})I_{2\times 2}$, where $V(\mathbf{r})$ is uniformly distributed in the interval $[-W/2, W/2]$, with W denoting the disorder strength. We find that the phase boundaries incline in opposite directions compared to the random flux case as shown in the Fig. 1(c) of the main text.

We note that the anisotropy from Fermi velocity ratio v_x/v_y also plays an important rule in these transitions. As illustrated in Fig. S4(b), the system undergoes topological phase transitions only within a proper regime of v_x/v_y . Such a sensitive dependence on Fermi velocity ratio is absent in the on-site disorder scenario. If we set $v_x = v_y$ but $b_x \neq b_y$ in Fig. S4(c), the topological random-flux insulator will not appear anymore. While for the case $b_x = b_y$, there is no WTI phase in the first place, and the CI is driven to a NI as increasing U_d [Fig. S4(d)].

Appendix S5: Critical features at the phase transition points

In this section, we present the critical scaling signatures at the phase transition points, specifically focusing on the transitions from a CI to a NI as a comparison. As already shown in Figs. 3(a) and 3(c) of the main text, the phase transition from a CI to a NI leads to the jump of Chern number from $C = 1$ to $C = 0$, accompanied by a transition in conductance from $G = \frac{e^2}{h}$ to $G = 0$.

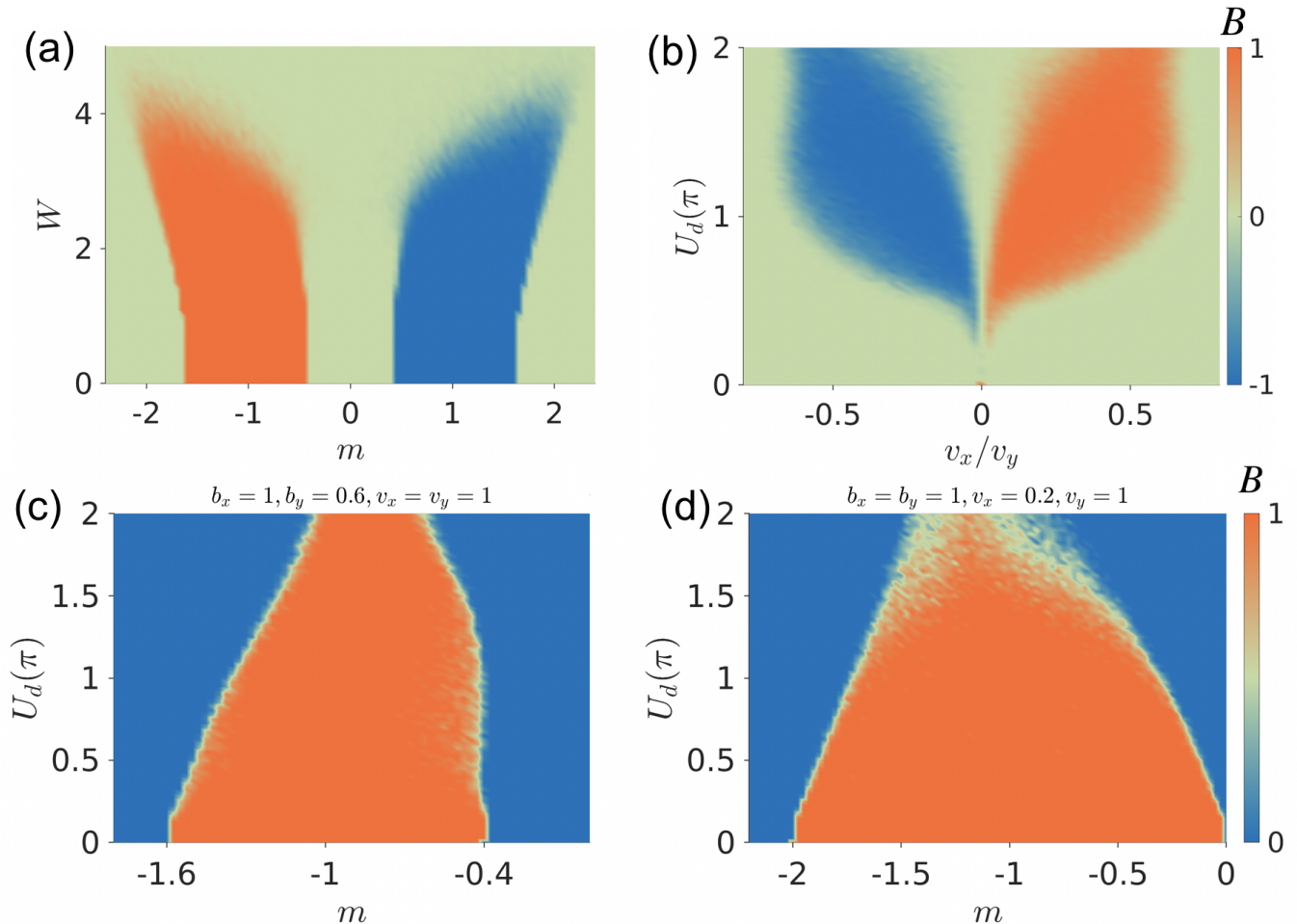


Figure S4. Phase diagram of the AWD model under different parameter settings. (a) Bott index as functions of on-site disorder strength W and mass m . No random flux is applied. Other parameters are: $b_x = 1, b_y = 0.6, v_x = 0.2$, and $v_y = 1$. (b) Bott index as a function random flux strength U_d and velocity ratio v_x/v_y for fixed mass term $m = -0.3$. Other parameters are $b_x = 1$ and $b_y = 0.6$. (c) Bott index as a function U_d and m for the condition of $b_x \neq b_y$ and $v_x = v_y$. (d) The same as (c) but with the condition of $b_x = b_y$ and $v_x \neq v_y$.

During the topological phase transition, a critical point emerges where the localization length diverges. To investigate this, we present the scaling behavior of normalized localization lengths as a function of random flux strength U_d in Fig. S5. We find that the critical points appear both along x direction [Fig. S5(a)] and y direction [Fig. S5(b)] at around $U_d \simeq 0.48\pi$, indicating the divergence of localization lengths along both x and y directions. This is attributed to the NI being trivial along both directions while CIs are nontrivial along both directions. These results show stark contrast with the quasi-critical phase points between the transitions of CIs and WTIs, where the localization length diverges only along one of the two directions.

Appendix S6: Local density of states for different phases under random flux

In this section, we present the local density of states along a representative phase line at $m = -0.3$ with increasing U_d : a WTI [Fig. S6(a)] is driven to a CI [Fig. S6(b)], and then to another WTI [Fig. S6(c)]. At $U_d = 0.1\pi$, the system resides a WTI with topological index $(C; \nu_x \nu_y) = (0; 10)$, thus the edge states appear only at y edges. At $U_d = 1.0\pi$, the system is driven to a CI with $C = 1$, where chiral edge states exist both along x and y edges. Further increasing to $U_d = 1.9\pi$, the system changes to another WTI with $(C; \nu_x \nu_y) = (0; 01)$, thus the edge states appear only at x edges.

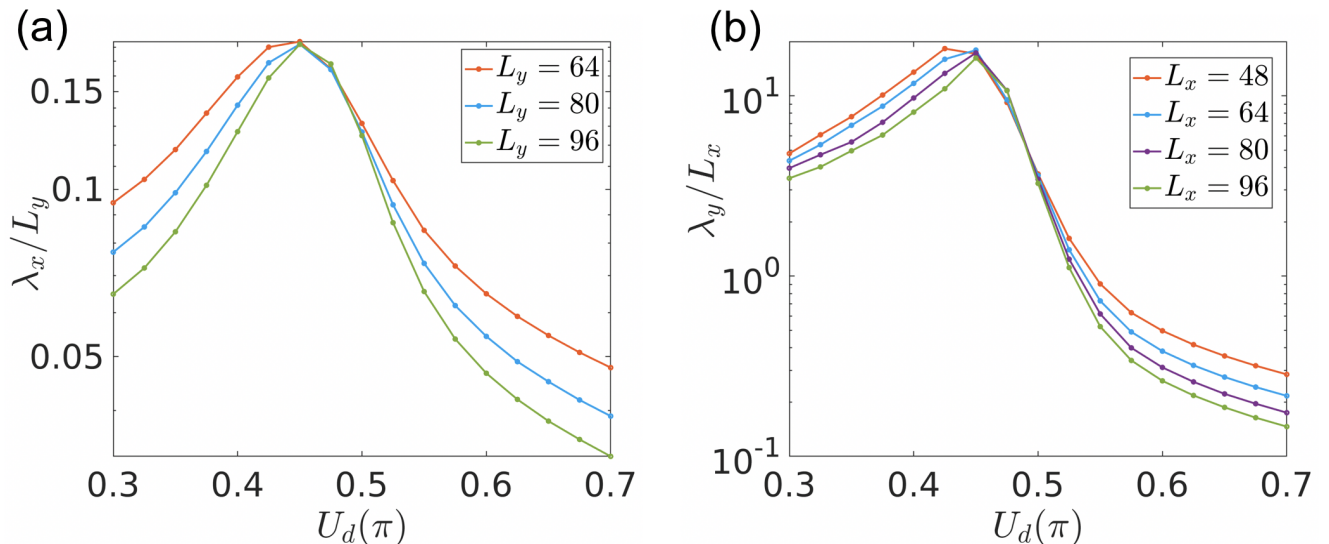


Figure S5. Localization length on a quasi-1D tube as a function of U_d . (a): along x direction; (b): along y direction. Other parameters are: $b_x = 1, b_y = 0.6, v_x = 0.2, v_y = 1$, and $m = -1.5$.

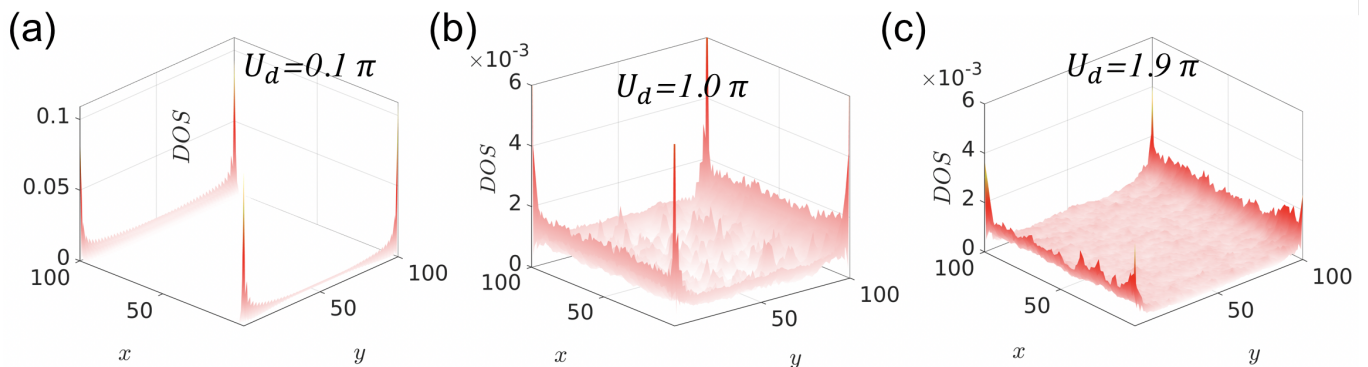


Figure S6. Averaged local density of states under different random flux strength U_d . (a) $U_d = 0.1\pi$, (b) $U_d = 1.0\pi$, and (c) $U_d = 1.9\pi$. Here 200 disorder configurations are taken. Other parameters are: $b_x = 1, b_y = 0.6, v_x = 0.2, v_y = 1, E = -0.04$, and $m = -0.3$.

Appendix S7: Robustness of topological random-flux insulator with on-site disorder

In this section, we show the robustness of topological random-flux insulators against on-site disorder potentials. To this end, we calculate the two-terminal conductance of the system with Chern insulators attached as leads. As illustrated in Fig. S7(a), the conductance plateau $G_x = \frac{e^2}{h}$ arising from the topological random-flux insulator persists to a finite on-site disorder strength $W \approx 0.8$ (green line). This is lower than the critical disorder strength $W \approx 1.7$ for an initially nontrivial CI (red line) because a smaller gap. For comparison, we also examine the transport along the y direction. For topological random-flux insulators induced within a finite window of U_d , the conductance reach a plateau $G_y = \frac{e^2}{h}$, as shown by the green line in Fig. S7(b). This conductance plateau $G_y = \frac{e^2}{h}$ survives the on-site disorder to a finite strength $W \approx 1.0$ [green line in Fig. S7(c)].

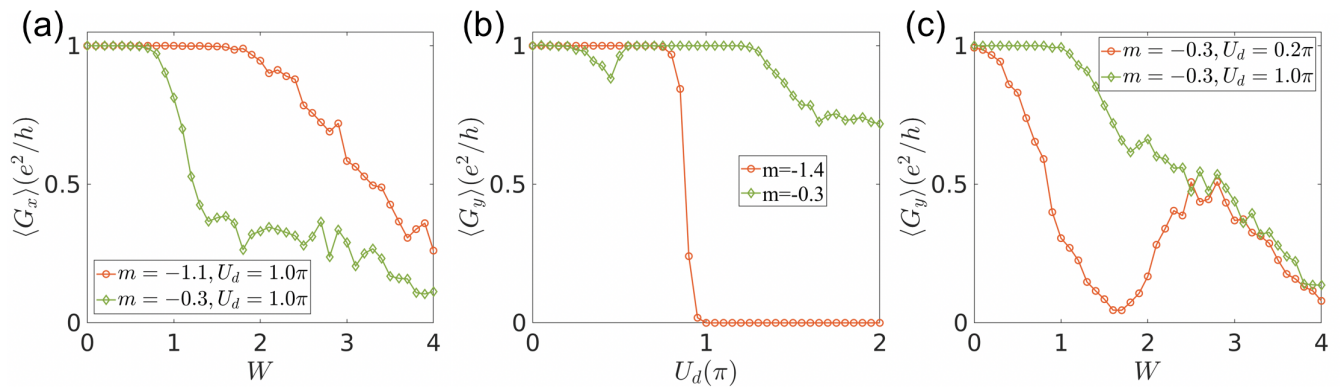


Figure S7. (a) Robustness of conductance G_x along x direction against on-site potential disorder strength W for different parameter m and fixed $U_d = 1.0\pi$. (b) Conductance G_y along y direction as a function of random flux strength U_d . (c) Robustness of conductance G_y along y direction against on-site potential disorder strength W for different parameter m and fixed $U_d = 1.0\pi$. Other parameters are: $b_x = 1, b_y = 0.6, v_x = 0.2$, and $v_y = 1$. Here we take 100 random configurations for all plots.